APPLIED PHYSICS

Flexible graphene photodetectors for wearable fitness monitoring

Emre O. Polat[1], Gabriel Mercier[1], Ivan Nikitskiy[1], Eric Puma[1], Teresa Galan[1], Shuchi Gupta[1], Marc Montagut[1], Juan José Piqueras[1], Maryse Bouwens[1], Turgut Durduran[1,2], Gerasimos Konstantatos[1,2]*, Stijn Goossens[1]*, Frank Koppens[1,2]*

Wearable health and wellness trackers based on optical detection are promising candidates for public health uses due to their noninvasive tracking of vital health signs. However, so far, the use of rigid technologies hindered the ultimate performance and form factor of the wearable. Here, we demonstrate a new class of flexible and transparent wearables based on graphene sensitized with semiconducting quantum dots (GQD). We show several prototype wearable devices that are able to monitor vital health signs noninvasively, including heart rate, arterial oxygen saturation (SpO_2), and respiratory rate. Operation with ambient light is demonstrated, offering low-power consumption. Moreover, using heterogeneous integration of a flexible ultraviolet (UV)–sensitive photodetector with a near-field communication circuit board allows wireless communication and power transfer between the photodetectors and a smartphone, offering battery-free operation. This technology paves the way toward seamlessly integrated wearables, and empowers the user through wireless probing of the UV index.

INTRODUCTION

The skin provides a unique interface for electronic devices to assess the current wellness and health status of our body (*1*–*3*). Almost all wearable devices for wellness monitoring and performance tracking use this window into the body to measure vital signs. The wearable electronics market currently encompasses a variety of device types and form factors, from smartwatches and smart clothing to head-mounted displays (*4*–*7*). While chemical and electrical interfaces have been brought forward (*8*), devices based on optical detection mechanisms offer the least invasive personal health tracking and hence have seen a very large adoption in the consumer market (*9*–*11*).

Optical vital sign monitoring is typically performed through photoplethysmography (PPG), which is a powerful, noninvasive technique that operates by sending light of a certain wavelength into the skin, optically detecting the volume change of blood vessels due to the cardiac cycle (*12*). PPG has already been implemented in commercial consumer devices to measure heart rate (HR) and arterial oxygen saturation (SpO_2) (*13*, *14*) and could, in principle, also be used for blood pressure (*15*–*17*), cardiac output (*18*, *19*), and many health signs that have vital information for personal well-being (*20*).

Aforementioned commercial PPG-based wearables are made out of discrete, rigid silicon photodiodes that cannot interface conformably with the skin and thereby reduce the accuracy of the data and limit the positions on the body where the wearable can be used. In the case of nonconformal optical measurements, motion of human body interferes with the pulse signal, leading the user to extract erroneous estimation of HR and related vital signs. Although alternate designs have been reported to prevent the motion artifacts, such as PPG ring on finger (*9*), HR sensor on the ear lobe (*21*), and forehead-mounted SpO_2 sensor (*22*), devices using bulky readout electronics and rigid sensors create the stigma about wearing a thick, visible device that monitor the wellness of the user (*23*–*25*). All these factors markedly lower the functionality and consumer adoption of these devices and create a high demand for sensing technologies with unique form factors and extended functionality. Therefore, conformable sensors with an aesthetically pleasing appearance that noninvasively measure a complete set of vital signs are the holy grail for the wearable field. To that end, many advancements have been reported such as artificial tattoo-like conformable electronic devices that provide wireless electrocardiogram monitoring (*1*), electronic skin that maps the strain (*26*), and stretchable memory and logic devices for wearable electronics (*27*). However, wearables where the active sensing components are completely flexible and transparent remained a great challenge.

Being transparent and flexible, graphene emerges as a viable material for wearable sensors. In particular, GQD (graphene sensitized with semiconducting quantum dots) photodetectors (PDs) (*28*) offer key benefits such as broadband wavelength sensitivity (300 to 2000 nm) and high responsivity due to a built-in photoconductive gain. This intrinsic photoconductive gain allows a design freedom that the nontransparent and bulky readout electronics can be placed away from the sensor, and therefore, transparency and form factor of the active sensing area can be preserved. We previously reported implementation of the GQD PD technology in broadband image sensors (*29*) and operation at submillisecond speeds and >80% efficiencies (*30*). Here, we integrate these PDs on flexible substrates and demonstrate a number of prototypes benefiting from the flexibility and the high and broadband sensitivity to light.

The assembly of chemical vapor deposition (CVD) graphene and a thin film of PbS colloidal quantum dots (QDs) (30 nm in thickness) forms the basis for the flexible PDs demonstrated in this work (Fig. 1, B and C). The flexible detectors are semitransparent (maximum recorded absorbance is 25% at 633 nm), and the resulting transparency can be tuned by changing the thickness of the QD layer controlling the trade-off between detector responsivity and transparency. While illuminated, absorbed photons create electron-hole pairs in the QD layer, which are then separated by the built-in electric field formed at the graphene-QD interface. One type of the separated carriers transfers to graphene, while oppositely charged carriers

[1]ICFO–Institut de Ciencies Fotoniques, The Barcelona Institute of Science and Technology, 08860 Castelldefels, Barcelona, Spain. [2]ICREA—Institució Catalana de Recerça i Estudis Avançats, Lluis Companys 23, 08010 Barcelona, Spain.
*Corresponding author. Email: gerasimos.konstantatos@icfo.eu (G.K.); stijn.goossens@icfo.eu (S.G.); frank.koppens@icfo.eu (F.K.)

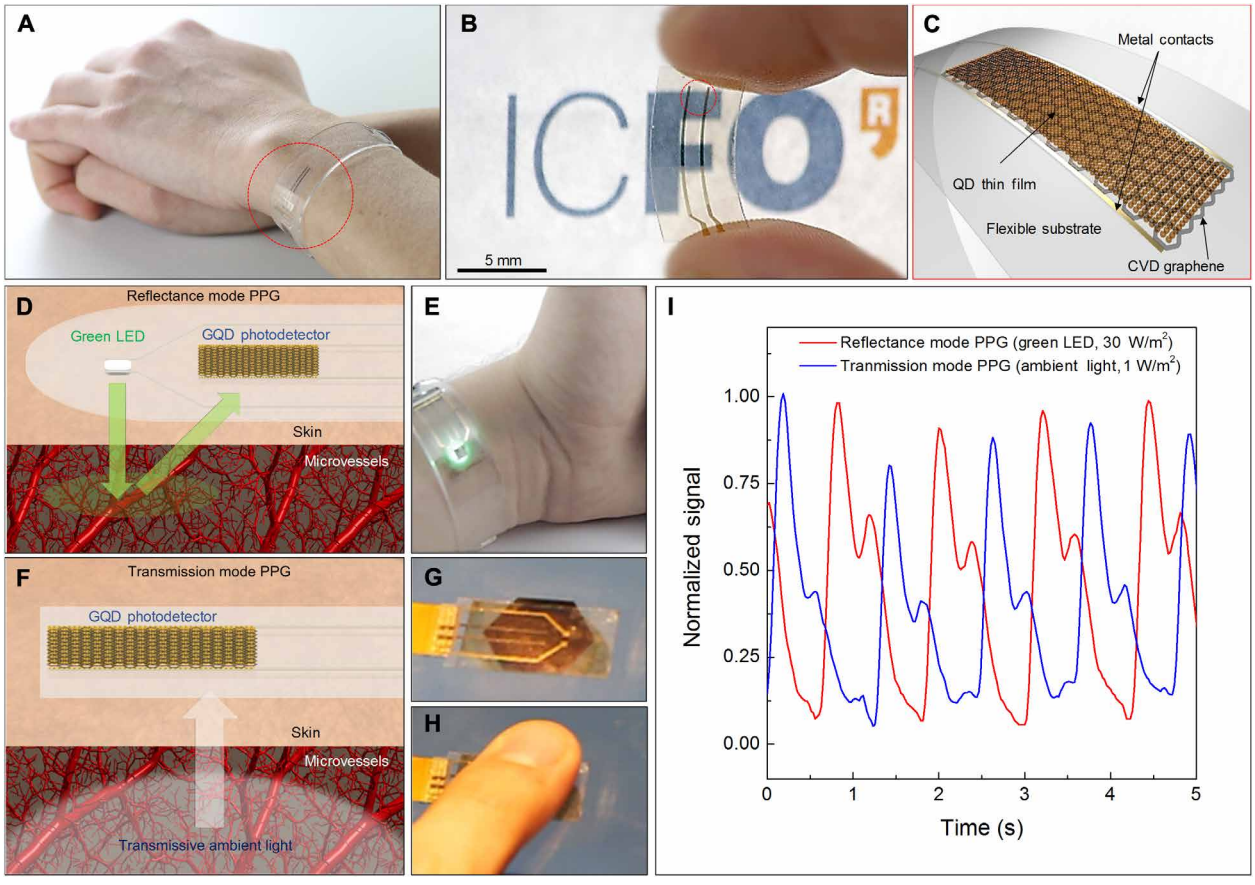

Fig. 1. Health-tracking prototypes based on GQD PDs. (**A**) Photograph of the flexible and transparent GQD PD integrated in HR monitoring bracelet. (**B**) Zoomed-in photograph of the flexible PD containing a 1-mm^2 graphene channel on the PEN substrate that is completely covered by a thin layer of PbS QDs (30 nm in thickness). The detector is visibly transparent and mechanically flexible. (**C**) Schematic illustration of the assembly of graphene and QDs on a flexible substrate. (**D**) Schematic of photoplethysmogram (PPG) in reflectance mode. Volumetric changes in the microvessels modulate the backscattered light reaching the GQD PD. (**E**) HR monitoring bracelet based on reflection mode PPG to extract vital signs from wrist. (**F**) Schematic of transmission mode PPG. Transmissive ambient light is modulated by the cardiac cycle and reaches the PD. (**G** and **H**) Photograph of the health patch on the mobile phone screen that uses transmission mode PPG to extract HR from finger. (**I**) Normalized PPG readings for transmission and reflectance modes of operation. High sensitivity and mechanical flexibility of GQD PDs allow health patches to operate accurately for long periods in both modes. Photo credit: Alina Hirschmann, ICFO–Institut de Ciencies Fotoniques.

remain trapped in the QD layer. This yields a measurable change in resistance (photoconductivity). We emphasize the photoconductive gain where the QD layer leads to the recycling of multiple charges in the biased graphene. For this reason, the responsivity of these PDs reaches high numbers, in this case of the order of 10^5 A/W.

This paper presents a number of flexible prototypes based on seamless integration of GQD PDs into health-tracking wearables, on a mobile phone screen and near-field communication (NFC) circuitry, to monitor vital health signs and the ultraviolet (UV) skin exposure wirelessly. We will first give an outlook of the prototypes and their real-time operation on human skin. Then, we will discuss in more detail the performance and durability of the flexible PDs and the prototypes based on them.

RESULTS

Flexible and transparent health patch

We have demonstrated the integration of a flexible PD in a flexible bracelet (Fig. 1, A and E) and on the mobile phone screen (Fig. 1, G and H), allowing users to track HR and respiration rate (RR) from a range of body locations. Prototypes shown in Fig. 1 are connected to external readout electronics to bias the PD and amplify the registered photo signal. In this way, we monitor and store the vital sign data in a connected device (i.e., smartphone, tablet, or computer). Demonstrated prototypes are able to operate in two different modes: transmission and reflectance PPG. In the reflectance mode, light sourced from an integrated green light-emitting diode (LED; 535 nm, 0.4 mW total optical power) is coupled into the skin (Fig. 1, D and E). The cardiac cycle changes the volume of the microvessels, which modulates the amount of the backscattered light reaching the PD (Fig. 1D). This modulation is registered by the PD and data are processed and monitored by an external readout circuit. We used the reflectance mode PPG to extract the HR of the user from the wrist (Fig. 1E and movie S1). On the other hand, we used the transmission mode PPG to monitor the HR of the user from a finger placed on the health patch (Fig. 1, G and H, and movie S2). In this case, the health patch uses the ambient light passing through the tissue, which then reaches the PD (Fig. 1F). Because of

the broadband wavelength sensitivity of the GQD PD, the health patch can operate in transmission mode using solely ambient light because light of higher wavelength penetrates further into the skin. This allows a wearable device to detect vital signs that require continuous tracking over a long time. Because of the absence of an external light source, the power consumption of the integrated wearables is very low and limited to the dissipation in the PD and the readout electronics. The recorded PPG signal for both modes and various light conditions is shown in Fig. 1I and fig. S1.

Graphene and QD assembly as a flexible PD

Here, we provide a detailed electro-optic characterization of the flexible GQD PDs. We have demonstrated a number of flexible device types including a macroscale PD on polyethylene terephthalate (PET) (Fig. 2A), a high-sensitivity PD on polyethylene naphthalate (PEN) (Fig. 2B, inset), and a PD on polyimide (Fig. 2D). For the latter, a gate that controls the carrier density in graphene was implemented, and therefore, the photoresponse can be tuned and optimized. We investigated the photosensitivity of all three devices and the mechanical robustness (see table S1). The PDs were lithographically patterned 1 mm × 1 mm GQD channels, and the change in photocurrent was measured while applying a constant DC bias voltage (V_{bias} = 1 V) through the metal contacts on both edges of the channel (see an example on a PEN substrate in Fig. 2B, inset). We measured the resistance R and extracted the photo-induced relative resistance change $\Delta R/R$ (Fig. 2B), and we found a clear power law: $\Delta R/R$ scales to the 0.88th power of irradiance. Beyond the linear threshold, there is a soft saturation effect that extends the dynamic range of the detector by several orders of magnitude (fig. S2). The observed dynamic range of the flexible PDs is limited by the noise of the measurement electronics, but we can deduce a lower bound of the linear dynamic range above 20 dB and a full dynamic range above 50 dB. The main noise contribution for GQD PDs is $1/f$ noise, which is empirically described by the Hooge relation (*29*). For our device, this noise was measured to be $\Delta R/R = 4.4 \times 10^{-7}$ at 1 Hz (fig. S3). From this, we infer a noise-equivalent irradiance (NEI) value of 3.7×10^{-11} W cm^{-2} (at 633 nm). To put this into context, starlight conditions correspond to an NEI of ~10^{-10} W cm^{-2}.

The mechanical stability of the flexible PDs was investigated through a protocol where we applied uniaxial tensile strain by bending them to 16 mm radius of curvature, up to 2000 active bending cycles. We recorded the photoresponse several times after multiple cycles (Fig. 2C). A slight initial change in the photoresponse (~15%) was observed for the first 50 cycles, which then reaches a relatively constant state (within ~10%) up to 2000 cycles. We expect that using thinner substrates would yield PDs with more flexibility.

To improve the sensitivity, speed, and tunability of the GQD PDs on flexible substrates, we implemented local gate control. As shown in (*28*–*30*) for gated devices on rigid substrates, a gate can control the speed and the efficiency of the charge separation at the QD-graphene interface. To use the gated PDs on flexible substrates, the 50-nm-thick aluminum gate metal was deposited directly on a polyimide substrate, which is then covered by 100-nm-thick Al_2O_3 through an atomic layer deposition process, and subsequently, the GQD PDs were fabricated on top (Fig. 2D). We observed strong tunability of the responsivity (Fig. 2E) and a maximum responsivity of ~10^5 A/W near charge neutrality point (CNP), allowing the detection of light intensities down to ~pW. We note the asymmetrical modulation of the responsivity because the gate tunes the graphene transconductance and the graphene-QD interface Schottky barrier at the same time (fig. S4) (*28*, *30*).

The dynamic response was investigated by sweeping the light modulation frequency at a fixed gate voltage (Fig. 2F and fig. S5). We observed that GQD PDs sustain high-frequency operation with a typical cutoff frequency in the order of 10 kHz. The inset in Fig. 2F shows a temporal response of a flexible GQD PD at 1 Hz, from which a response time of 50 μs is extracted (fig. S6).

Vital sign monitoring via GQD health patches

We now proceed to provide in more detail the extraction of various vital signs by using transmission mode PPG depicted in Fig. 1 (F to H). To provide a complete mobile readout, we connected the health patch to a Bluetooth module that processes and sends the data to a mobile phone wirelessly (Fig. 3A). As a daily life object, smartphones represent a regularly preferred platform to individual data loggers in the context of personal heath monitoring (*23*). We developed a software that allows the user to monitor HR by placing the finger on the sensor that is integrated on the mobile phone screen (Fig. 3B and movie S2). When ambient indoor light transmits through the finger, it is modulated by the volumetric change of the blood vessels and then reaches the detector. In this way, we can provide accurate measurements of HR, SpO_2, and RR continuously over long periods.

To optically extract the SpO_2, we recorded the pulse of an individual for visible (633 nm) and near-infrared (940 nm) wavelengths. For the wavelengths of 660 and 940 nm, the difference in the extinction coefficient between the oxygenated and non-oxygenated hemoglobin is highest, allowing a precise extraction of the SpO_2 from the blood pulse traces in Fig. 3C (*31*).

Next, we evaluated the accuracy in HR measurements, by taking simultaneous HR measurements from both the GQD health patch (HR_{GQD}) and a state-of-the-art (HR_{SoA}) PPG sensor used in the clinical setting (Fig. 3D). We correlated the simultaneous HR measurements by using an algorithm to identify and count blood pulse peaks registered by both measurements. We found a strong linear correlation with a concordance correlation coefficient of $\rho = 0.98$ over continuous 5-min measurement. We further examined the accuracy by a Bland-Altman plot analysis (Fig. 3E). The variations in between the limit of agreement (±LoA) state the high probability that the methods do not disagree. Our data fall predominantly within these limits.

From the photodetection signal, we could also extract the RR simultaneously with the HR. RR provides information on the respiratory status, which can be an important indicator to determine various complications from respiratory depression to tract infections (*32*). The act of respiration has a strong effect on PPG measurements, changing the baseline amplitude modulation periodically (fig. S8), and thus can be detected from a frequency analysis, as shown in Fig. 3F. The observed high-intensity peaks in the Fourier transform of the PPG signal correspond to dominant RRs and HRs of the individual, respectively, 17 breaths per minute and 72 bpm (Fig. 3F). Dynamic changes in RR and HR reveal themselves as harmonics around the dominant peaks in the Fourier transform (fig. S9). By using an algorithm, we monitored a dynamic RR range of 12 to 20 breathe per minute and an HR range of 60 to 80 bpm for this particular measurement (Fig. 3F). A Bland-Altman plot for the extracted RR (Fig. 3G) yields a good agreement together with the correlation plot (Fig. 3G, inset). Extraction of the RR is done by an algorithm that

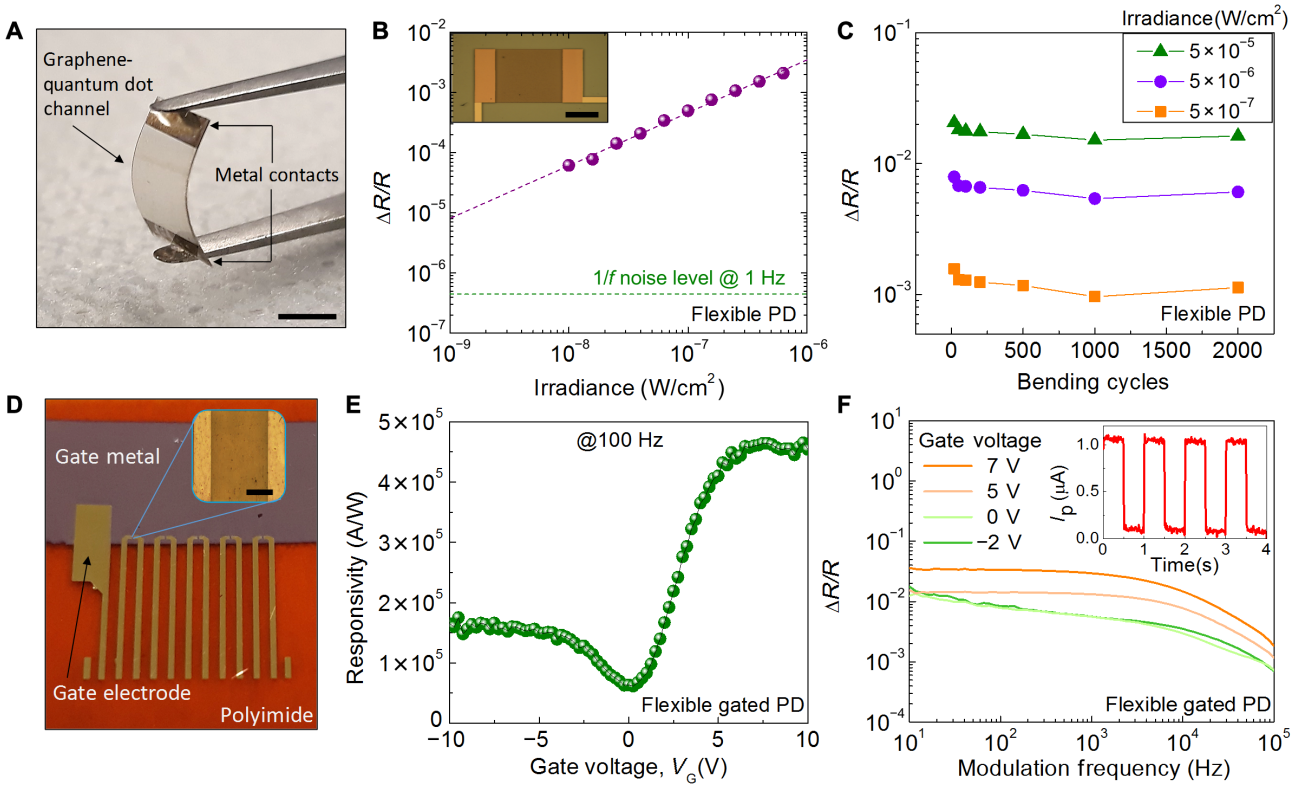

Fig. 2. Electro-optical and mechanical characterization of the GQD PDs on flexible polymer substrates. (**A**) Photograph of macroscale PD on the PET substrate. Scale bar, 5 mm. (**B**) Photo-induced resistance change ($\Delta R/R$) with respect to irradiance at 633 nm. Horizontal dashed line represents the noise floor of the device, which is measured to be 4.4×10^{-7} and corresponds to an NEI value of 3.7×10^{-11} W cm^{-2}. Inset shows an individual GQD PD on the PEN substrate. Scale bar, 500 μm. (**C**) Mechanical stability of the flexible PD on the PEN substrate. Change in photoresponse due to applied uniaxial strain is minimal over 2000 cycles. (**D**) Photograph of the gated PDs on polyimide. Series of PDs were implemented on a gate structure containing a 50-nm Al covered by a 100-nm Al_2O_3 dielectric layer. Contact electrodes are extended along the substrate for interconnects. Inset shows a zoomed-in image of the GQD channel on the gate structure. Scale bar, 50 μm. (**E**) Responsivity versus applied gate voltage. Gate provides control on the speed, responsivity, and the transferred charge type. (**F**) Dynamic response of the detector for fixed gate voltages. Flexible PDs sustain high-frequency operation with a typical cutoff frequency on the order of 10^4 Hz. The inset shows the temporal response at 633 nm from which the response time is extracted to be 50 μs. Photo credit: Emre O. Polat, ICFO–Institut de Ciencies Fotoniques.

divides the 5-min measurement into frames of 100 s and identifies the change in the frequency of dominant RR peaks. We believe that with more efficient algorithms, the RR correlation between the state-of-the-art capnograph and the GQD health patch would yield values closer to 1 as for the HR measurement.

Heterogeneous integration and wireless UV exposure monitoring

A very important aspect of flexible GQD PD technology is its capability of integration on previously fabricated flexible Printed circuit board (PCBs). To show the promises of the approach, we integrated the GQD PD with a commercially available flexible NFC circuit board to demonstrate a UV skin exposure monitoring patch. The integrated system allows battery-free operation and wireless transfer of data and power between smartphone and PD.

Heterogeneous integration of the GQD PD on NFC circuitry has been realized with the incorporation of a conformal thermoplastic layer in between the PD and the substrate (Fig. 4A). Then, 50-nm-thick Ti/Au lines are deposited to both ends of the GQD PD to provide the electrical contact to the built-in circuitry including a microprocessor, a digital converter, and an NFC antenna. As shown in Fig. 4B, the system maintains a two-way communication in between the UV patch and the mobile phone, allowing battery-free operation and data transfer. The environmental UV intensity changes are registered by the integrated GQD assembly, causing a resistance modulation in graphene, which is then converted into a digital signal and modulated by the built-in microcontroller to be sent wirelessly to a mobile phone via amplitude shift key (ASK) modulation. The mobile phone receives the digitalized data and then processes and displays it on the screen. The power needed to operate the GQD assembly and the built-in electronics of the patch is sent wirelessly by using coupled antennae coils through a high-frequency (13.56 MHz) electromagnetic field for both power and data transfer (Fig. 4B). The UV patch operates with a low-power consumption (140 μA/MHz, 16 μA on standby), offering a highly efficient UV detection system that can be attached to clothing or skin for monitoring the harmful effects of the sun on the skin. We encapsulated the integrated patch with a plastic PET cap including a flexible short-pass light filter to block the unwanted light spectrum (>400 nm) and to provide extra protection against the mechanical stress (Fig. 4C). The developed mobile app displays the actual UV index of the environment and the remaining recommended exposure time on smartphone's screen when the phone is brought into close proximity to the UV patch (Fig. 4C).

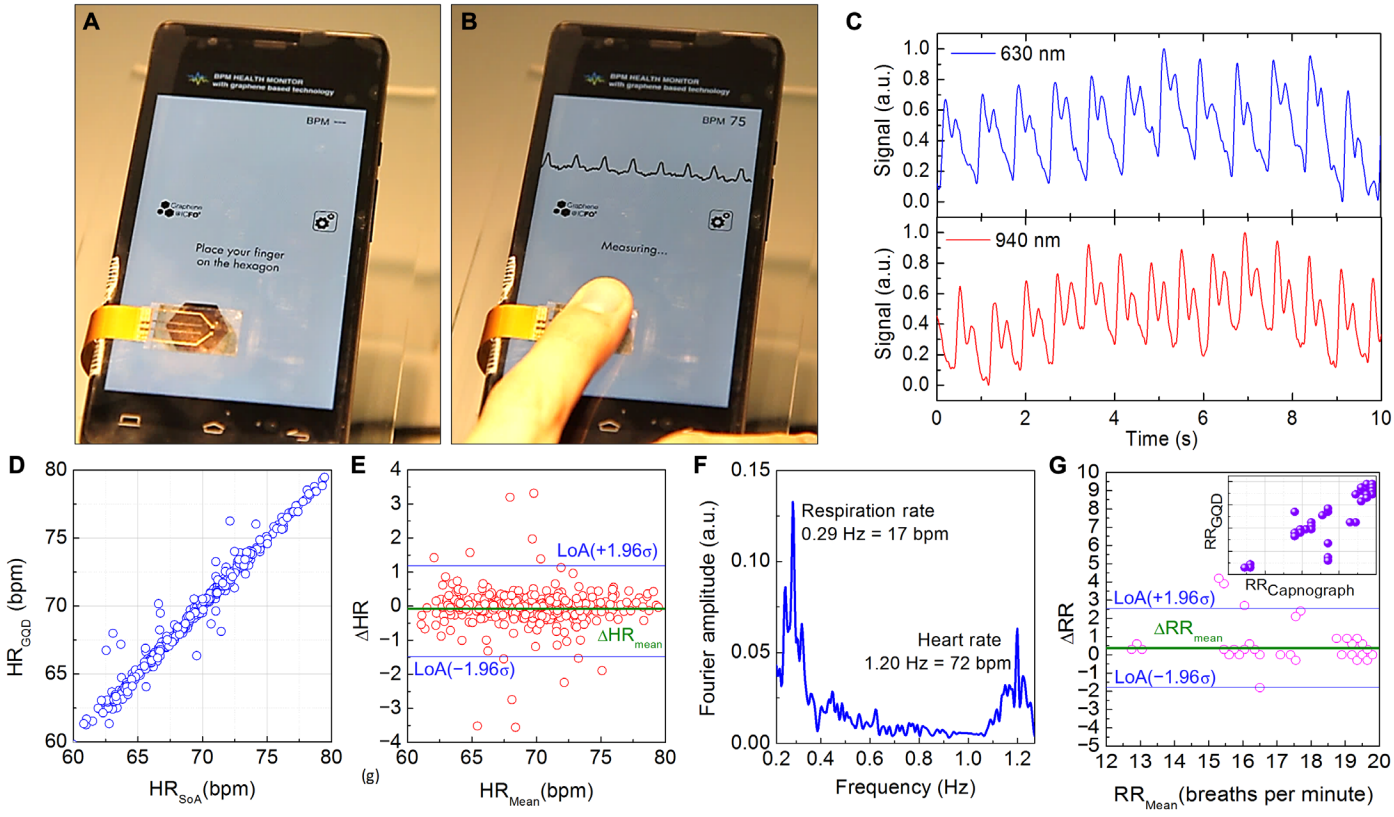

Fig. 3. HR and RR measurements by GQD health patches. (**A**) Flexible and transparent health patch on the mobile phone screen. Software is in an idle state. (**B**) Blood pulse monitoring from the user's finger. Two-terminal health patch connects to a mobile readout unit, which processes and sends the data to the mobile phone via Bluetooth. The developed software allows monitoring of the HR in real time and displays the PPG trace. (**C**) PPG trace for visible and near-infrared wavelengths. Multi-wavelength absorption of the GQD channel presents compatibility for optical measurements of SpO_2. (**D**) Correlation plot of measurements from the health patch (HR_{GQD}) and a state-of-the-art PPG sensor used in the clinical setting (HR_{SoA}) (Nellcor OxiMax SpO_2 module, Medtronic Capnostream 20p). The data from the two devices yield a concordance correlation coefficient of 0.988, representing a high correlation in between two simultaneous measurements. (**E**) Bland-Altman plot analysis of the health patch. The green line represents the mean difference (ΔH_{Mean}) of simultaneous measurements taken from both devices with a value of −0.078. The top and bottom blue lines represent the SD of both measurements (±1.96σ) that set the limit of agreement (LoA) of the measurements with the values of (−1.48, 1.18). The variations in between the limit of agreement (±LoA) state the high probability that the methods do not disagree. (**F**) Fourier transform of the recorded PPG. High-intensity peaks at 0.29 and 1.20 Hz represent the dominant RR and HR of the individual over 5 min of recording, which correspond to 17 breathe per minute and 72 bpm respectively. Harmonics at 0.25 and 0.33 Hz correspond to RRs of 15 and 20 bpm, and HR harmonics at 1.16 and 1.22 Hz correspond to 69 and 73 bpm. (**G**) Bland-Altman plot analysis for the extracted RR proving the good agreement with the values of $\Delta H_{Mean} = 0.39$ and LoA = (−1.79, 2.53) for the GQD health patch and state-of-the-art capnograph in the clinical setting (Medtronic Capnostream 20p). Inset shows the correlation plot showing the linear agreement with a concordance correlation coefficient of 0.8421. Photo credit: Stijn Goossens, ICFO—Institut de Ciencies Fotoniques.

UV radiation is often classified as UVA, UVB, and UVC, which correspond to wavelength intervals of 315 to 380 nm, 280 to 315 nm, and 200 to 280 nm, respectively. Direct skin absorption of shortwave UV (UVB-UVC) creates genotoxic substances due to the associated high energy (4 to 6 eV) (*33*). Using the integrated PD, we performed measurements at 285 nm to mimic the radiation that causes sunburn, and correlated the irradiance scale to the UV steps of 25 mW/m^2 according to the Diffey weighted average (*34*). The UV patch is able to register the irradiance changes with a resolution of 0.1 mW/m^2, and the output NFC signal of the UV patch exhibits a linear dependence with respect to intensity of incident UV light (Fig. 4D). In this way, we wirelessly monitor the active UV index changes in the surrounding environment.

DISCUSSION, CONCLUSION, AND OUTLOOK

GQD PDs in flexible and wearable devices and integration of them with predesigned electronic components unlock a new platform for detecting vital signs (such as HR, RR, and SpO_2) noninvasively on skin, as well as probing the environmental UV index wirelessly. The ability of inconspicuous integration makes the flexible GQD assembly a strong contender for incorporation in garments, jewelry, headwear, and footwear. This also enables sensing applications on curvy surfaces in which the detector must detect a portion of the light while still transmitting most of it, such as detectors on flexible displays.

We report a number of prototype devices such as health patches integrated on a mobile phone screen and in the transparent bracelets that are able to that are able to provide real-time and continuous PPG reading. Operation with ambient light has been demonstrated, allowing low-power consumption in the integrated wearables and therefore monitoring of health markers continuously over long periods. Moreover, we demonstrated a wearable UV patch by the heterogeneous integration of the GQD PDs onto the NFC antenna circuitry. The UV patch enables wireless transfer of both power and data, and thus battery-free operation to sense the environmental UV index. In general, our technology provides a scalable route for integration of

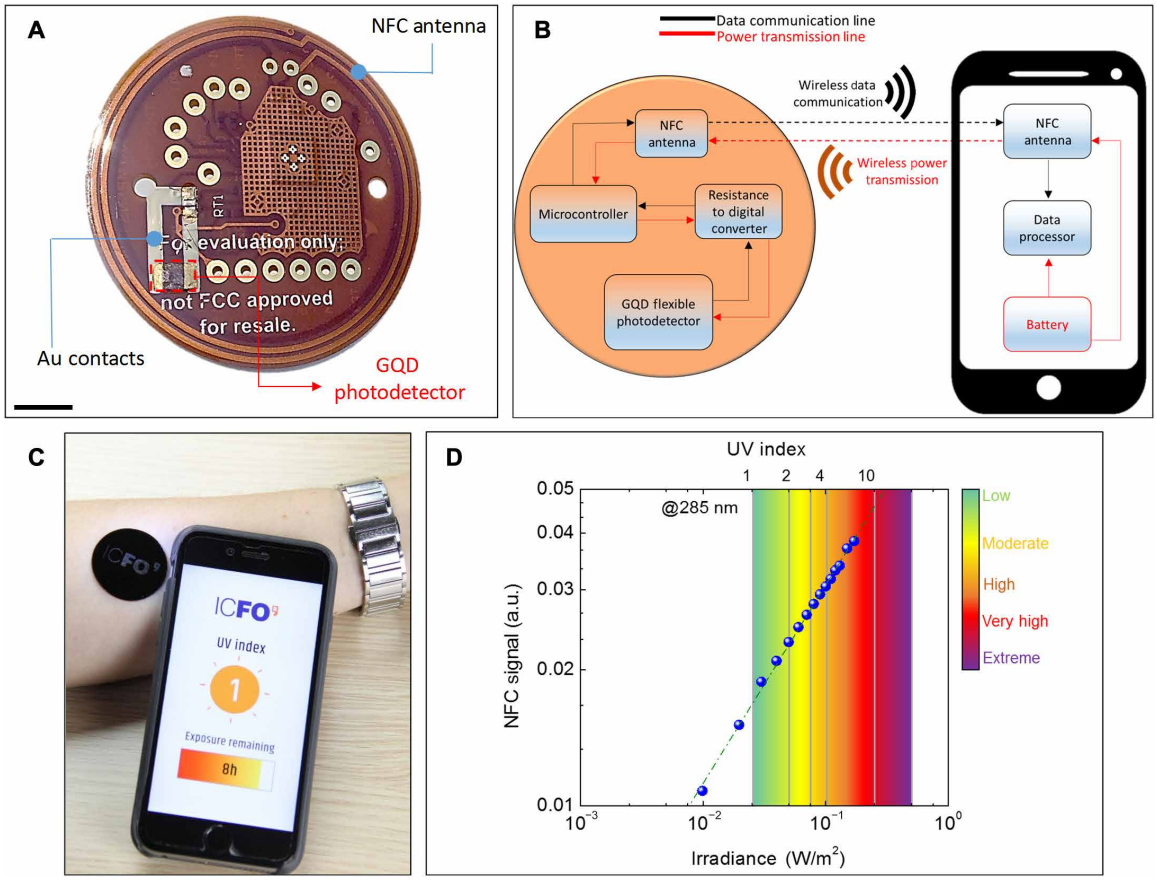

Fig. 4. Wireless and battery-free UV monitoring patch. (**A**) Photograph of the GQD-UV patch. GQD assembly was heterogeneously integrated onto a commercially available NFC patch (TIDM-RF430-TEMPSENSE, Texas Instruments), and the electrical connection between PD and the chip is obtained by deposited metal lines. Scale bar, 10 mm. (**B**) Block diagram of the wireless and battery-free UV monitoring system. NFC provides two-way communication by inductively powering the patch and wirelessly sending the data to smartphone. (**C**) Mobile UV index monitoring via UV patch placed on the arm. The patch uses a flexible short-pass filter on the front side that blocks the wavelengths greater than 400 nm, allowing an accurate monitoring of the environmental UV index. The developed software displays the actual UV index and informs the user about recommended remaining exposure time. (**D**) Modulation of output NFC signal with respect to irradiance at 285 nm. High sensitivity of 1 mW/m^2 allow accurate and wireless UV index measurement. The color scale shows the severity of the UV exposure according to the Diffey weighted average. Photo credit: Alina Hirschmann, ICFO-Institut de Ciencies Fotoniques.

graphene into fully flexible wearable circuits to enhance form, feel, durability, and function.

The built-in gain of our detectors bypasses the current requirement of the presence of an amplifier at close proximity. This allows a large degree of design freedom while performing precise measurements on the finger and the arm but potentially also on the forehead, foot, or even the chest. The broad wavelength detection range enables extending the number of vital signs that can be measured. We envision sensing even more vital signs such as hydration (*35*–*38*) and muscle microvascular blood oxygenation (*39*–*42*).

Recent progress in two-dimensional (2D) semiconductors such as MoS_2 and WS_2 for logic and analog electronics opens up a promising pathway toward the realization of a fully integrated flexible platform that is constructed purely from (flexible) 2D materials. MoS_2 transistors can be potentially used as multiplexer switches (*43*–*45*) to address different sensors and as preamplifiers for the data acquisition system, while graphene-based materials can function as the RFID (radio-frequency identification) or Bluetooth antennae (*46*–*48*). Currently, the final transparency and flexibility of the GQD PD integrated system may be hindered by the readout electronics consisting of relatively opaque and rigid circuitry. An all-2D material–based wearable would provide a monolithic system with an advanced form factor that benefits from enhanced flexibility and (semi-) transparency of 2D materials while maintaining exceptionally high (opto-)electronic quality. Mass-produced and low-cost devices are within reach for this flexible wearable platform, as it is fully compatible with scalable CVD growth and roll-to-roll transfer processes (*49*–*52*).

MATERIALS AND METHODS

Fabrication of flexible PDs and the health patch prototypes

Metal contact pads were formed on 125-μm-thick biaxial oriented PEN (Teijin Teonex PEN films) by electron-beam evaporation of 2-nm Ti and thermal evaporation of 20-nm Au in high vacuum (10^{-7} torr; Lesker LAB18 evaporation system) followed by a lift-off process. Then, CVD-grown graphene on copper (4 cm × 6 cm; Graphenea S.A.) was transferred from the deionized water surface using a polymethyl methacrylate (PMMA) support layer and dried overnight to remove trapped water. PMMA residues were removed by hot acetone and mild solvent stripper. Samples were rinsed in isopropyl alcohol (IPA) and water and then dried in a vacuum desiccator. We investigated the quality and the uniformity of graphene

on flexible polymer substrates by large-area Raman mapping (fig. S10), which indicates that the intrinsic quality is reasonable (i.e., mobility, ~1000 cm^2/Vs). Lithographic masks for graphene channels were fabricated by laser writing. Oxygen plasma etching was used to pattern and isolate the graphene channels. The sensitizing thin film of PbS colloidal QD layers was formed by spin coating on top of the graphene layer, followed by a 1,2-ethanedithiol ligand exchange. The synthesis of PbS colloidal QDs was performed using a Schlenk line under inert conditions (*53*). GQD channels in the demonstrated prototypes were laminated with a conformable PET cap to prevent any mechanical damage that may arise from skin interaction.

Fabrication of gated flexible PDs

A 125-μm-thick polyimide sheet (DuPont Kapton HN) was surface-cleaned in acetone and IPA and then dried overnight at 80°C in the laboratory oven. Then, the 50-nm-thick Al gate metal was thermally evaporated in high vacuum through a shadow mask. We deposited by atomic layer deposition a 100-nm-thick Al_2O_3 dielectric layer at 250°C with a base pressure of 250 mtorr using trimethylaluminum (TMA) as a precursor. Ti (2 nm) and Au (50 nm) were evaporated as electrical contacts on top of Al/Al_2O_3 layers. Then, CVD graphene was transferred and patterned through oxygen plasma. Samples were annealed at 350°C in H_2 environment to remove the PMMA residues of wet transfer. Then, the photosensitizing QD layer fabrication was applied as indicated above.

Electro-optic characterization

Flexible PDs were characterized in an optical probe station by applying 1 V of source-drain voltage under the illumination of various light intensities. Diode lasers (633 and 1150 nm) were connected to an attenuator to achieve a broad range of intensities. During the photosensitivity measurements, a drain amplifier was used to improve the output signal amplitude and a low-pass filter was used to reduce electronic noise (fig. S3).

UV index measurements

A 285-nm UV LED was used as a light source. Various intensities were obtained through natural density filters. The corresponding UV indices were calculated using the Diffey weighted average (*34*). Each intensity step was measured individually and calibrated with a UV power meter (S120VC, Thorlabs Standard Photodiode Power Sensor). Then, GQD UV patches were tested under various intensities at certain distances from the light source. Interference of higher wavelengths (>400 nm) was blocked with optical filters and cover shields.

SUPPLEMENTARY MATERIALS

Supplementary material for this article is available at http://advances.sciencemag.org/cgi/content/full/5/9/eaaw7846/DC1

Fig. S1. PPG readings of GQD Health Patch under various light conditions for the same applied bias.
Fig. S2. Flexible and transparent GQD assembly on PEN and the dynamic range of flexible GQD PDs.
Fig. S3. Noise characteristics of flexible GQD PDs.
Fig. S4. Gate modulation of flexible gated GQD PDs.
Fig. S5. Photosensitivity for various operation frequencies.
Fig. S6. Temporal response of the flexible GQD PD at 633 nm.
Fig. S7. Photoresponse of flexible GQD PDs at near-infrared wavelength.
Fig. S8. Continuous PPG reading by GQD health patch.
Fig. S9. Simultaneous measurements of GQD health patch and state-of-the-art capnograph.
Fig. S10. Large-area Raman spectroscopy mapping of graphene on flexible polymer substrates.
Table S1. Demonstrated device types and their specifications.
Movie S1. GQD bracelet (reflection mode PPG).
Movie S2. GQD health patch on the mobile phone screen (transmission mode PPG).

REFERENCES AND NOTES

1. D.-H. Kim, N. Lu, R. Ma, Y.-S. Kim, R.-H. Kim, S. Wang, J. Wu, S. M. Won, H. Tao, A. Islam, K. J. Yu, T.-i. Kim, R. Chowdhury, M. Ying, L. Xu, M. Li, H.-J. Chung, H. Keum, M. McCormick, P. Liu, Y.-W. Zhang, F. G. Omenetto, Y. Huang, T. Coleman, J. A. Rogers, Epidermal electronics. *Science* **333**, 838–843 (2011).
2. A. J. Bandodkar, W. Jia, J. Wang, Tattoo-based wearable electrochemical devices: A review. *Electroanalysis* **27**, 562–572 (2015).
3. J. Choi, R. Ghaffari, L. B. Baker, J. A. Rogers, Skin-interfaced systems for sweat collection and analytics. *Sci. Adv.* **4**, eaar3921 (2018).
4. S. Majumder, T. Mondal, M. Deen, Wearable Sensors for remote health monitoring. *Sensors* **17**, 130 (2017).
5. M. Stoppa, A. Chiolerio, Wearable electronics and smart textiles: A critical review. *Sensors* **14**, 11957–11992 (2014).
6. H. Li, L. Trutoiu, K. Olszewski, L. Wei, T. Trutna, P.-L. Hsieh, A. Nicholls, C. Ma, Facial performance sensing head-mounted display. *ACM Trans. Graph.* **34**, 47 (2015).
7. R. Rawassizadeh, B. A. Price, M. Petre, Wearables: Has the age of smartwatches finally arrived? *Commun. ACM* **58**, 45–47 (2015).
8. A. J. Bandodkar, I. Jeerapan, J. Wang, Wearable chemical sensors: Present challenges and future prospects. *ACS Sens.* **1**, 464–482 (2016).
9. H. H. Asada, P. Shaltis, A. Reisner, S. Rhee, R. C. Hutchinson, Mobile monitoring with wearable photoplethysmographic biosensors. *IEEE Eng. Med. Biol. Mag.* **22**, 28–40 (2003).
10. J. Heikenfeld, A. Jajack, J. Rogers, P. Gutruf, L. Tian, T. Pan, R. Li, M. Khine, J. Kim, J. Wang, J. Kim, Wearable sensors: Modalities, challenges, and prospects. *Lab Chip* **18**, 217–248 (2018).
11. A. Henriksen, M. Haugen Mikalsen, A. Z. Woldaregay, M. Muzny, G. Hartvigsen, L. A. Hopstock, S. Grimsgaard, Using fitness trackers and smartwatches to measure physical activity in research: Analysis of consumer wrist-worn wearables. *J. Med. Internet Res.* **20**, e110 (2018).
12. J. Allen, Photoplethysmography and its application in clinical physiological measurement. *Physiol. Meas.* **28**, R1–R39 (2007).
13. T. Tamura, Y. Maeda, M. Sekine, M. Yoshida, Wearable photoplethysmographic sensors—Past and present. *Electronics* **3**, 282–302 (2014).
14. A. Kamišalić, I. Fister, M. Turkanović, S. Karakatič, Sensors and functionalities of non-invasive wrist-wearable devices: A review. *Sensors* **18**, 1714 (2018).
15. I. C. Jeong, J. I. Ko, S. O. Hwang, H. R. Yoon, A new method to estimate arterial blood pressure using photoplethysmographic signal. *Conf. Proc. IEEE Eng. Med. Biol. Soc.* **1**, 4667–4670 (2006).
16. X. Xing, M. Sun, Optical blood pressure estimation with photoplethysmography and FFT-based neural networks. *Biomed. Opt. Express* **7**, 3007–3020 (2016).
17. H. Shin, S. D. Min, Feasibility study for the non-invasive blood pressure estimation based on ppg morphology: Normotensive subject study. *Biomed. Eng. Online* **16**, 10 (2017).
18. Q. Y. Lee, S. J. Redmond, G. S. H. Chan, P. M. Middleton, E. Steel, P. Malouf, C. Critoph, G. Flynn, E. O'Lone, N. H. Lovell, Estimation of cardiac output and systemic vascular resistance using a multivariate regression model with features selected from the finger photoplethysmogram and routine cardiovascular measurements. *Biomed. Eng. Online* **12**, 19 (2013).
19. N. Daimiwal, M. Sundhararajan, Non invasive measurement and analysis of cardiac output for different age group using PPG sensor. *Int. J. Comput. Appl.* **1**, 25–28 (2016).
20. M. Elgendi, On the analysis of fingertip photoplethysmogram signals. *Curr. Cardiol. Rev.* **8**, 14–25 (2012).
21. K. Shin, Y. Kim, S. Bae, K. Park, S. Kim, A novel headset with a transmissive ppg sensor for heart rate measurement. *IFMBE Proc.* **23**, 519–522 (2009).
22. Y. Mendelson, R. J. Duckworth, G. Comtois, A wearable reflectance pulse oximeter for remote physiological monitoring. *Conf. Proc. IEEE Eng. Med. Biol. Soc.* **1**, 912–915 (2006).
23. S. Patel, H. Park, P. Bonato, L. Chan, M. Rodgers, A review of wearable sensors and systems with application in rehabilitation. *J. Neuroeng. Rehabil.* **9**, 21 (2012).
24. C. Farrington, Wearable technologies and stigma in diabetes: The role of medical aesthetics. *Lancet Diabetes Endocrinol.* **4**, 566 (2016).
25. K. Bodine, F. Gemperle, Effects of functionality on perceived comfort of wearables, in *Proceedings of Seventh IEEE International Symposium on Wearable Computers* (IEEE, 2003).
26. J. Kim, M. Lee, H. J. Shim, R. Ghaffari, H. R. Cho, D. Son, Y. H. Jung, M. Soh, C. Choi, S. Jung, K. Chu, D. Jeon, S.-T. Lee, J. H. Kim, S. H. Choi, T. Hyeon, D.-H. Kim, Stretchable silicon nanoribbon electronics for skin prosthesis. *Nat. Commun.* **5**, 5747 (2014).
27. D. Son, J. H. Koo, J.-K. Song, J. Kim, M. Lee, H. J. Shim, M. Park, M. Lee, J. H. Kim, D.-H. Kim, Stretchable carbon nanotube charge-trap floating-gate memory and logic devices for wearable electronics. *ACS Nano* **9**, 5585–5593 (2015).

28. G. Konstantatos, M. Badioli, L. Gaudreau, J. Osmond, M. Bernechea, F. P. Garcia de Arquer, F. Gatti, F. H. L. Koppens, Hybrid graphene–quantum dot phototransistors with ultrahigh gain. *Nat. Nanotechnol.* **7**, 363–368 (2012).
29. S. Goossens, G. Navickaite, C. Monasterio, S. Gupta, J. J. Piqueras, R. Pérez, G. Burwell, I. Nikitskiy, T. Lasanta, T. Galán, E. Puma, A. Centeno, A. Pesquera, A. Zurutuza, G. Konstantatos, F. Koppens, Broadband image sensor array based on graphene–CMOS integration. *Nat. Photonics* **11**, 366–371 (2017).
30. I. Nikitskiy, S. Goossens, D. Kufer, T. Lasanta, G. Navickaite, F. H. L. Koppens, G. Konstantatos, Integrating an electrically active colloidal quantum dot photodiode with a graphene phototransistor. *Nat. Commun.* **7**, 11954 (2016).
31. M. Nitzan, A. Romem, R. Koppel, Pulse oximetry: Fundamentals and technology update. *Med. Devices Evid. Res.* **7**, 231–239 (2014).
32. P. S. Addison, J. N. Watson, M. L. Mestek, J. P. Ochs, A. A. Uribe, S. D. Bergese, Pulse oximetry-derived respiratory rate in general care floor patients. *J. Clin. Monit. Comput.* **29**, 113–120 (2015).
33. Z. Kuluncsics, D. Perdiz, E. Brulay, B. Muel, E. Sage, Wavelength dependence of ultraviolet-induced DNA damage distribution: Involvement of direct or indirect mechanisms and possible artefacts. *J. Photochem. Photobiol. B Biol.* **49**, 71–80 (1999).
34. A. F. McKinlay, B. L. Diffey, A reference action spectrum for ultra-violet induced erythema in human skin. *CIE J.* **6**, 17–22 (1987).
35. L. E. Armstrong, Assessing hydration status: The elusive gold standard. *J. Am. Coll. Nutr.* **26**, 575S–584S (2007).
36. E. Berardesca; European Group for Efficacy Measurements on Cosmetics and Other Topical Products (EEMCO), EEMCO guidance for the assessment of stratum corneum hydration: Electrical methods. *Skin Res. Technol.* **3**, 126–132 (1997).
37. J. M. Schmitt, Device and method for monitoring body fluid and electrolyte disorders, U.S. Patent 6,591,122 (2003).
38. S. M. Shirreffs, Markers of hydration status. *Eur. J. Clin. Nutr.* **57**, S6–S9 (2003).
39. N. B. Hampson, C. A. Piantadosi, Near infrared monitoring of human skeletal muscle oxygenation during forearm ischemia. *J. Appl. Physiol.* **64**, 2449–2457 (1988).
40. R. Boushel, C. A. Piantadosi, Near-infrared spectroscopy for monitoring muscle oxygenation. *Acta Physiol. Scand.* **168**, 615–622 (2000).
41. R. Belardinelli, T. J. Barstow, J. Porszasz, K. Wasserman, Changes in skeletal muscle oxygenation during incremental exercise measured with near infrared spectroscopy. *Eur. J. Appl. Physiol. Occup. Physiol.* **70**, 487–492 (1995).
42. T. Hamaoka, K. K. McCully, V. Quaresima, K. Yamamoto, B. Chance, Near-infrared spectroscopy/imaging for monitoring muscle oxygenation and oxidative metabolism in healthy and diseased humans. *J. Biomed. Opt.* **12**, 062105 (2007).
43. S. Wachter, D. K. Polyushkin, O. Bethge, T. Mueller, A microprocessor based on a two-dimensional semiconductor. *Nat. Commun.* **8**, 14948 (2017).
44. B. Radisavljevic, A. Radenovic, J. Brivio, V. Giacometti, A. Kis, Single-layer MoS_2 transistors. *Nat. Nanotechnol.* **6**, 147–150 (2011).
45. M. Choi, Y. J. Park, B. K. Sharma, S.-R. Bae, S. Y. Kim, J.-H. Ahn, Flexible active-matrix organic light-emitting diode display enabled by MoS_2 thin-film transistor. *Sci. Adv.* **4**, eaas8721 (2018).
46. X. Huang, T. Leng, M. Zhu, X. Zhang, J. C. Chen, K. H. Chang, M. Aqeeli, A. K. Geim, K. S. Novoselov, Z. Hu, Highly flexible and conductive printed graphene for wireless wearable communications applications. *Sci. Rep.* **5**, 18298 (2015).
47. X. Huang, T. Leng, M. Zhu, X. Zhang, J. C. Chen, K. H. Chang, A. K. Geim, K. S. Novoselov, Z. Hu, Binder-free highly conductive graphene laminate for low cost printed radio frequency applications. *Appl. Phys. Lett.* **106**, 203105 (2015).
48. J. Perruisseau-Carrier, Graphene for antenna applications: Opportunities and challenges from microwaves to THz, in *Loughborough Antennas and Propagation Conference* (2012), 1–4.
49. S. Bae, H. Kim, Y. Lee, X. Xu, J.-S. Park, Y. Zheng, J. Balakrishnan, T. Lei, H. R. Kim, Y. I. Song, Y.-J. Kim, K. S. Kim, B. Özyilmaz, J.-H. Ahn, B. H. Hong, S. Iijima, Roll-to-roll production of 30-inch graphene films for transparent electrodes. *Nat. Nanotechnol.* **5**, 574–578 (2010).
50. T. Hesjedal, Continuous roll-to-roll growth of graphene films by chemical vapor deposition. *Appl. Phys. Lett.* **98**, 133106 (2011).
51. T. Kobayashi, M. Bando, N. Kimura, K. Shimizu, K. Kadono, N. Umezu, K. Miyahara, S. Hayazaki, S. Nagai, Y. Mizuguchi, Y. Murakami, D. Hobara, Production of a 100-m-long high-quality graphene transparent conductive film by roll-to-roll chemical vapor deposition and transfer process. *Appl. Phys. Lett.* **102**, 023112 (2013).
52. Z.-Y. Juang, C.-Y. Wu, A.-Y. Lu, C.-Y. Su, K.-C. Leou, F.-R. Chen, C.-H. Tsai, Graphene synthesis by chemical vapor deposition and transfer by a roll-to-roll process. *Carbon* **48**, 3169–3174 (2010).
53. A. Mihi, F. J. Beck, T. Lasanta, A. K. Rath, G. Konstantatos, Imprinted electrodes for enhanced light trapping in solution processed solar cells. *Adv. Mater.* **26**, 443–448 (2014).

Acknowledgments: We thank J. Hollman and K. Sexton for input in design of the experiment, C. Monasterio for the technical contribution to measurement electronics setup and computer interfaces, J. Fischer for technical contribution to vital signs monitoring, and Graphenea Semiconductor SLU for providing CVD graphene samples. All individuals providing personal data confirmed the ethical approval by signing the informed consent form. **Funding:** We acknowledge the support from the Spanish Ministry of Economy and Competitiveness through the "Severo Ochoa" Programme for Centres of Excellence in R&D (SEV-2015-0522); the Fundacio Cellex Barcelona, Generalitat de Catalunya through the CERCA program; and the Agency for Management of University and Research Grants (AGAUR) 2017 SGR 1656, as well as the ERC Proof-of-concept GRAPHEALTH with ref. 713659 (to F.K.) and 2017 SGR 1380 (to T.D.). T.D. also acknowledges support from the Obra Social "la Caixa" Foundation (LlumMedBcn). Furthermore, the research leading to these results received funding from the European Union Seventh Framework Programme under grant agreement no. 785219 Graphene Flagship. **Author contributions:** T.D., G.K., S.Go., and F.K. conceived the experiments and provided supervision and guidance during the execution of the work. E.O.P., I.N., and E.P. designed and fabricated the devices. E.O.P., G.M., I.N., E.P., J.J.P., and M.B. performed all the experiments and measurements. E.O.P. and G.M. performed the data analysis. S.Gu. synthesized materials. T.G. characterized the materials and contributed to device fabrication. M.M. created the rendered images and developed the user interfaces of mobile measurements. E.O.P., G.M., S.Go., and F.K. wrote the manuscript with inputs from all authors. All authors provided input to data analysis, discussed the results, and assisted in manuscript preparation. **Competing interests:** The authors declare that they have no competing interests. **Data and materials availability:** All data needed to evaluate the conclusions in the paper are present in the paper and/or the Supplementary Materials. Additional data related to this paper may be requested from the authors.

Submitted 24 January 2019
Accepted 19 August 2019
Published 13 September 2019
10.1126/sciadv.aaw7846

Citation: E. O. Polat, G. Mercier, I. Nikitskiy, E. Puma, T. Galan, S. Gupta, M. Montagut, J. J. Piqueras, M. Bouwens, T. Durduran, G. Konstantatos, S. Goossens, F. Koppens, Flexible graphene photodetectors for wearable fitness monitoring. *Sci. Adv.* **5**, eaaw7846 (2019).